High-performance conformal sensors employing single-crystal silicon nanomembranes

Xiaochuan Xu [1,*], Harish Subbaraman [1,*], Swapnajit Chakravarty [1], and Ray T. Chen[2]

[1]Omega Optics, Inc., 8500 Shoal Creek Blvd, Building 4, Suite 200, Austin, TX 78757, USA

[2]Dept. Electrical and Computer Engineering, The University of Texas at Austin, 10100 Burnet Rd, PRC/MER 160, Austin, TX 78758, USA.

Author e-mail address: xiaochuan.xu@omegaoptics.com, chen@ece.utexas.edu

ABSTRACT

We demonstrate light-weight, conformal, and high-performance flexible sensors fabricated on a large area (>2 cm x 2 cm) silicon nanomembrane transferred onto a flexible substrate. Linear L13 photonic crystal microcavities are designed to provide high quality factors on the flexible platform. Subwavelength grating (SWG) couplers are employed in order to enable efficient light coupling to the device using a single mode fiber. Photonic crystal tapers are implemented at the strip-photonic crystal waveguide interfaces to minimize loss. Preliminary chemical sensing data suggests a sensitivity of 75nm/RIU. Bending tests are further performed in order to demonstrate sensitivity-independent operation.

Key words: photonic crystal waveguide, subwavelength grating, silicon nanomembranes, flexible photonics.

1. INTRODUCTION

In recent years, there has been a growing interest in inorganic nanomembrane based photonics on unconventional substrates. For example, with the stamp printing method, Dr. Weidong Zhou's group at the University of Texas at Arlington were able to transfer Fano resonators onto different substrates.[1, 2] These approaches can be categorized as surface normal photonic devices. Compared to the surface normal devices, it is much more difficult to transfer in-plane photonic devices onto unusual substrates because photonic devices have more complicated geometry, although a few attempts have been made. In our previous research, we stamp printed photonic devices onto Kapton films, which is the first demonstration of in-plane single crystal photonic devices on flexible substrates.[3] To boost the yield, a pedestal structure is designed and tailored to adjust the van der Waals force between the released device and the silicon handle so that the force is strong enough to hold the device in place, but at the same time small enough to be peeled up by an elastomeric stamp. The process demonstrates a satisfying yield, but it is very complicated and has to be adjusted to accommodate different device designs to achieve the best transfer yield. Prof. Mo Li's group at the University of Minnesota has demonstrated the transfer of ring resonator and Mach-Zehnder interferometer onto Polydimethylsilxoane(PDMS) substrate based on an anchor structure formed by controlled wet etch of silicon dioxide.[4] It requires a precise control of the wet etching of silicon dioxide (SiO_2) layer on the SOI. Liquid nitrogen is used to control the etching temperature. After transfer, the device is bonded to the PDMS substrate via van der Waals force, which is weak. Therefore, the device would not be reliable enough. Another disadvantage of the transfer process is that the size of the silicon dioxide is very important. It needs to be strong enough to hold the device and weak enough to be broken during the peeling

Silicon Photonics IX, edited by Joel Kubby, Graham T. Reed, Proc. of SPIE Vol. 8990, 89900U
 · doi: 10.1117/12.2039888

procedure. As a result, the width of the device that can be transferred has to be identical. It limits the method to transferring single mode waveguide based devices, like ring resonator and Mach-Zehnder interferometer, demonstrated in this paper. One of the side effects is that the light has to be coupled into single mode waveguide directly. The coupling efficiency is extremely poor due to the large mode mismatch. Another attempt to demonstrate flexible photonic device was to fabricate photonic device directly on amorphous silicon which is directly deposited onto flexible substrates.[5] The drawback of this method is that the optical characteristic of amorphous silicon is not as good as single crystal silicon. Besides, patterning photonic devices on soft material is not a reliable procedure especially when the feature size is small.

This paper summarizes our progress in transferring photonic devices onto flexible substrates. We are able to transfer a large area silicon nanomembrane defect freely onto flexible substrates. To demonstrate the capabilities of transferring intricate photonic devices, L13 photonic crystal microcavities have been transferred onto flexible substrates. The quality factor of this cavity is ~ 9000, which is comparable with that on SOI, indicating the high quality of the transferred silicon nanomembrane. Bending test has been conducted to thoroughly investigate the behavior of the cavity. This photonic crystal micro cavity can be used for a myriad of different applications. As an example, the refractive index sensing capability has been verified. It exhibits a comparable sensitivity. The sensitivity remains quite consistent under different bending radii.

2. FABRICATION

The L13 microcavity was fabricated on commercially available silicon-on-insulator (250 nm silicon, 3 μm buried oxide layer, and 650 mm silicon handle). The wafer was cleaved into 2 cm×2 cm chips, and the chips were cleaned though piranha bath. Hexamethyldisilazane (HMDS) was spun coated at 4000 rpm for 35s. Electron beam resist (ZEP 520a) was spun coated at 6000 rpm for 35s, giving a resist of 350 nm thick. The pattern was transferred on to the resist by JBL 6000, and then to the silicon layer through reactive ion etching (HBr/Cl_2). The resist was stripped off by PG remover and a piranha bath.

The transfer process flow is described in Fig. 1. As illustrated in Fig. 1a, the Kapton film is cleaned with Acetone and Methanol, and dried with nitrogen. To simplify the following process, the Kapton film is mounted on a rigid substrate, such as silicon. A layer of 5 μm thick SU-8 is spin casted on the Kapton film and baked under 90^{o}C for 20 mins. The fabricated L13 cavity is cleaned by piranha bath. The native oxide is removed by 1:6 buffered oxide etchant (BOE). A layer of 5 μm SU-8 is spun coated and also baked under 90^{o}C for 20 mins. The extended baking time assures the solvent is completely evaporated, which is crucial to a successful bond. Besides, SU-8 has extraordinary self-planarization capability under a temperature above its glass transition temperature (64 ^{o}C [6, 7]). Long term baking could minimize the edge bead effect as well as other thickness variations.[7]

Since both the Kapton and the SOI are not transparent to ultra-violet (UV) light, the SU-8 layer cannot be cured in an ordinary way. This problem can be solved by curing the SU-8 first and then heating the sample up to the glass transition temperature (~ 180 ^{o}C, depends on different crosslink level) to let the SU-8 reflow. However, since the materials involved have quite different coefficients of thermal expansion, the stack could be cracked during the bonding thermal cycle under such a high temperature. The crosslink of SU-8 relies on the generation of acid upon UV exposure as a result of protolysis of triarylsulfonium hexafluorantimonium, the cationic photointiator. Thus, one layer of partially cured SU-8 and one layer of uncured SU-8 were brought together. The partially cured SU-8 will provide the acid and the uncured SU-8 reflows when being heated up, which makes bonding with a simple set up possible. The UV exposure dose is around 75 mJ/cm^2. Pressure is applied afterwards through a home-made bonder. The material stack is mounted between two thick Pyrex glass slides. The steel ball and the Belleville washer spread the point force generated by the thumb screw onto the thick top Pyrex glass plate. This structure forms a gradient pressure distribution with a higher pressure at the center and a lower at the edges. This

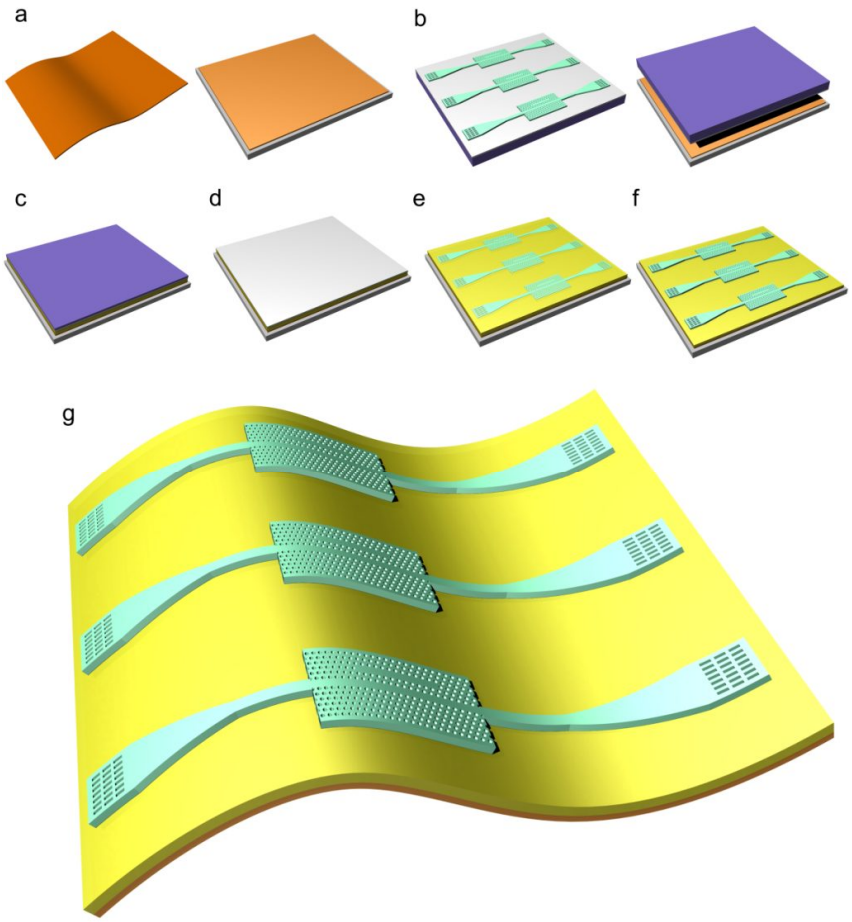

Figure 1 Tranfer Process. To make the figures more clear, the peripheral silicon is not shown. a. clean and mount a Kapton film on a silicon chip. b. flip over and bond a SOI chip onto the Kapton film with SU-8 as adhesive layer. c. thin down the silicon handle to ~ 100 ㎜. d. using deep silicon etching to etch away the remaining ~ 100 ㎜ silicon. e. remove the box layer with HF. f. remove the SU-8 filling into the holes of photonic crystal to enhance the sensitivity. g. peel off the Kapton film.

distribution avoids the formation of air cavities in between the two SU-8 layers. As the polymer flows, the pressure decreases, which can be compensated by the thermal expansion of the Belleville washers. The sample is kept in a 90 ^{o}C oven for 12 hours to allow for polymer to reflow and to squeeze out the trapped air bubbles.

After bonding, the silicon handle is removed by DRIE, as described in Figs. 1c and 1d. Since DRIE generates heat at a high speed, the carrier wafer, on which the sample sits, is kept at ~ 10 ^{o}C through Helium flow underneath. However, the thermal conductivities of SU-8 and Kapton film are merely 0.2 W/mK and 0.52 W/mK, respectively, and thus the heat generated by the etching process cannot be dissipated fast enough. Consequently, a significant temperature gradient builds up between the top surface and the silicon carrier substrate, subjecting the sample to cracking. The mismatch of the coefficients of thermal expansion (CTE) further aggravates the thermal problem. To control the thermal budget, the silicon handle is mechanically polished down to ~100 μm, as shown in Fig. 1c, to shorten the etching time. The etching recipe is also carefully modified to accommodate the thermal requirements. The conventional Bosch process contains three steps: polymer deposition, polymer etching, and silicon etching. The polymer deposition time is set to 5 s to protect the perimeter of the membrane, because the charges accumulated on the Kapton surface bend the electric field and etch silicon and SU-8 from the side, possibly causing undercut. The anisotropic polymer etching step is skipped in this application because the quality of the perimeter is not important. The polymer is removed during the silicon etching step. The inductively coupled plasma (ICP) power is carefully tuned to keep it slightly above the threshold of maintaining plasma to reduce the heat generation rate to match the heat dissipation rate. However, this adjustment sacrifices the etch rate. To compensate it, a long silicon etching time of 30 s is used in each cycle. The silicon etch rate of this recipe is around 2.7 μm/cycle with a selectivity of ~80 over silicon dioxide. The 3 μm BOX is used as a stopping layer to protect the SiNM underneath, and it can be removed by hydrofluoric (HF) acid etching afterwards.

Before removing the BOX layer, photoresist is applied on both the bottom and the top of the sample except the BOX region to protect the bonding between Kapton and the SiNM. Instead of immersing the whole sample into HF solution, which causes delamination because HF attacks the bonding between the sample and polymer, a few droplets of HF are applied on the BOX directly. The surface tension of the silicon dioxide constrains the solution within the SiNM without flowing over. The drawback is that etching speed could fall as the HF concentration decreases. Thus, a few more drops of HF needs to be added to maintain necessary HF concentration. The process is shown by Fig. 1e. After transfer, the thickness of the SU-8 is measured to be around 9.5 μm. The thickness variation across the entire chip is ~200 nm, possibly caused by the uneven pressure during the bonding step. The holes of the photonic crystal structures are filled with SU-8 which reduces the sensitivity of the photonic crystal cavity. Another reactive ion etching is used to remove the SU-8 filled into the holes, as shown in Fig. 1f. Finally, the Kapton film is peeled off from the silicon carrier, as shown in Fig. 1g. The transferred silicon nanomembrane devices are shown in Fig. 2a.

3. DEVICE CHARACTERIZATION

3.1 Schematics of the transferred L13 microcavity

The schematic of the transferred L13 cavity is illustrated in Fig. 2b. The total length of the device is 4 mm. Subwavelength grating couplers are used for input and output coupling. The width of the grating coupler is 10 μm. Two sections of 500 μm long adiabatic tapers are used to bridge the grating coupler and the single mode waveguide. A 30 μm long, 500 nm wide single mode waveguide is used to filter out the high order mode generated in the taper. After that, the single mode waveguide is tapered up to match the width of the photonic crystal waveguide. The insets of Fig. 3 show the SEM pictures of the transferred L13 microcavity and the subwavelength grating couplers.

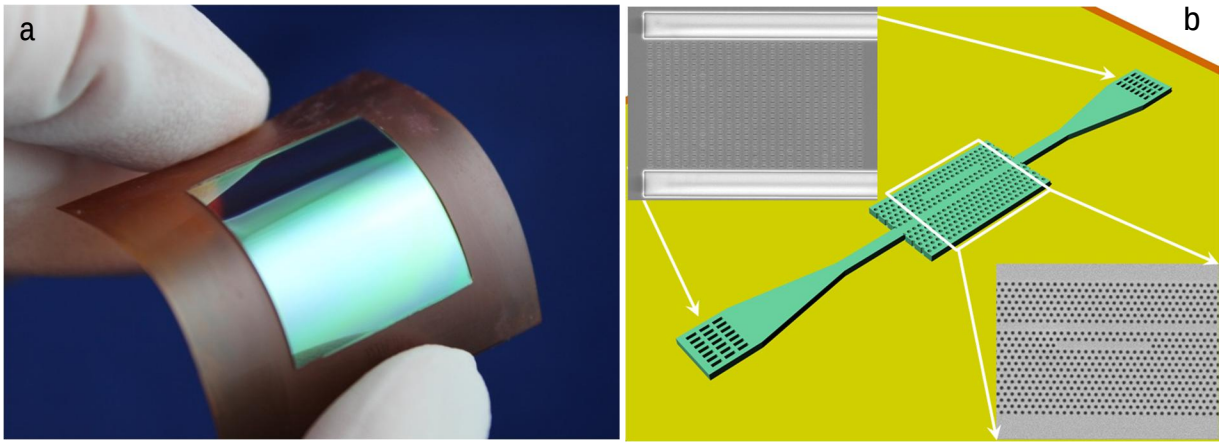

Figure 2 (a) L13 microcavity after being transferred on the Kapton film. The silicon nanomembrane after transfer is 2 cm×2 cm. (b) Schematic of the transferred L13 microcavity. The total length of the device is 4 mm. Subwavelength grating couplers are used as input and output grating couplers. Inset: SEM pictures of the subwavelength grating coupler and the L13 microcavity.

3.2 Introduction to the testing set up

The testing set up is shown in Fig. 3a. The transferred SiNM L13 cavity is mounted on the two jaws of a caliper. The caliper is mounted on a stage by two screws. As illustrated by the cartoon in the inset, through moving the transition jaw, the film can be buckled up and down. The position of a transition jaw can be controlled with an accuracy of 0.01 mm, which enables a precise scanning of bending radius. The testing method could be simplified as a two dimension model shown in Fig. 3b and c. The flexible composite film is comprised of three layers, 125 μm Kapton film, 10 μm SU-8, and 250 nm silicon nanomembrane. One end of the film is fixed and the other is movable. Assuming the film has a length of L, and the total thickness of the film is h, the bending shape of the film can be estimated as:[8]

$$W = W_0 \sin\left(\frac{\pi x}{L - dL}\right) \tag{1}$$

where

$$w_0 = \frac{2}{\pi}\sqrt{\frac{dL}{L} - \frac{\pi^2 h^2}{12L^2}} \tag{2}$$

Therefore the bending radius at the peak point can be calculated by:

$$R = \frac{L}{2\pi\sqrt{\frac{dL}{L} - \frac{\pi^2 h^2}{12L^2}}} \tag{3}$$

The light is coupled into the devices through subwavelength grating couplers. The input fiber is a polarization maintaining fiber (PMF), and the output fiber is a single mode fiber (SMF). Both fibers are mounted in fiber chucks which are fixed by chuck holders on 20 degree wedges. The tilting angle of fibers can be controlled within a range of 10~30 degrees to accommodate the bending tests. The axis of the PMF is aligned with the grating coupler. Light from a broadband source is polarized by a polarizer and connected to the PMF through a fiber connector. Light from output grating coupler is collected by the SMF and analyzed by optical spectrum analyzer (OSA).

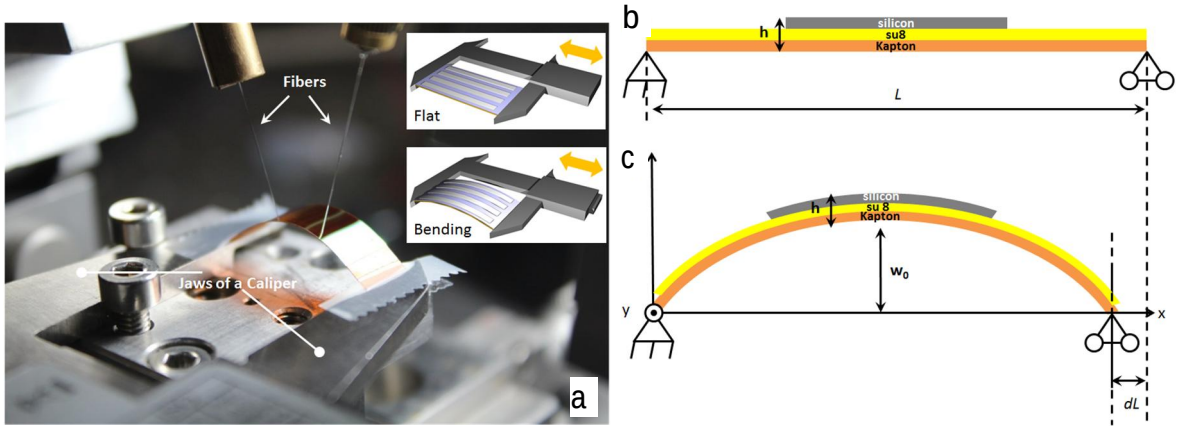

Figure 3 The testing set up. The transferred L13 cavity is mounted on the two jaws of a caliper. Moving the transitional jaw can buckle the film up or down. Light is coupled into the cavity through subwavelength grating couplers. The input and output fibers are held by fiber chucks, which is hold by fiber chuck holder mounted on titling stages.

3.3 The performance of grating couplers on flexible substrates

Coupling light into and out of the transferred devices is a challenging and crucial task. End-fire coupling is a straight forward option but not a wise one for flexible silicon photonic devices. On one hand the facet is extremely difficult to prepare,[3] which may turn the simple solution into a difficult one. On other hand, the coupling efficiency is close to zero due to the large mode mismatch. An alternative is grating couplers. However, the conventional grating coupler requires multiple lithography and etching steps to reduce the index contrast and increase directionality. Besides, the one dimension periodic structure is not mechanically strong enough. Subwavelength grating couplers provide a viable option.[9, 10] The low index region of subwavelength grating couplers is comprised of artificial nanostructures, which are more robust. The entire grating can be fabricated together with other photonic components with an efficiency which is comparable to those that demand multiple lithography and alignment steps. Since the holes of subwavelength grating couplers could be completely filled or partially filled with SU-8, the grating coupler needs to work properly in both situations.

The subwavelength structures can be considered as a uniform material according to the effective medium theory. So the 3D problem is simplified into a 2D problem. The SU-8 layer is rather thick, and the index contrast between SU-8 (1.575) and Kapton (1.79) is much smaller than that between silicon dioxide (1.45) and silicon (3.476). The effect of bottom cladding can be ignored. The simulation and optimization procedure is similar to that in reference [9] and [10], so it would not be reiterated here. The optimized subwavelength refractive index n_{sub} is 2.45. The grating period Λ is 0.69 μm. The subwavelength period is 0.390 μm, and the width of the air hole is 0.39 μm. The 2D FDTD simulation of fiber to grating coupling is shown in Fig. 4a. The tilting angle is ~9.4°. The simulation demonstrates a peak coupling efficiency of -3.2 dB at the wavelength of 1550 nm. The transmission spectrum of the grating couplers after transfer is also shown in the same figure. The grating coupler has a coupling efficiency of ~4.4 dB at 1536.7 nm. The discrepancy on coupling efficiency and peak wavelength is caused by the Kapton substrate and the dimension variation induced by the transfer process. When the holes are infiltrated with

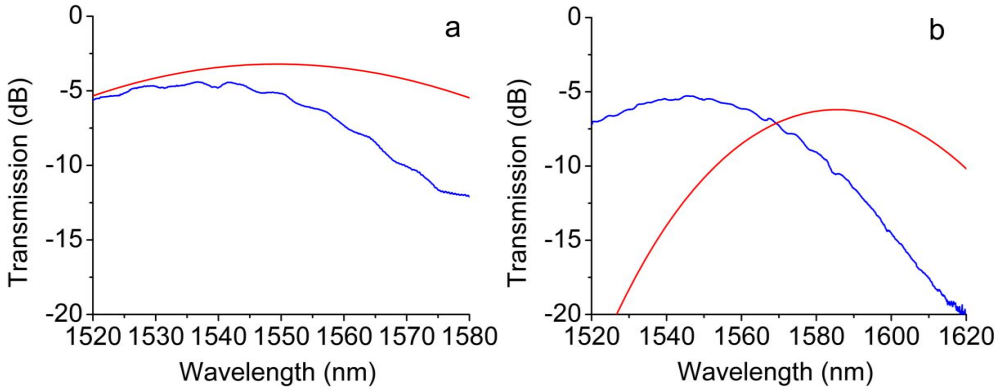

Figure 4 The simulation and experimental results of subwavelength grating couplers after transfer. a. the holes are not filled with SU 8. b. the holes are filled with SU 8. Red: simulation curve. Blue: experimental results.

SU-8, the refractive index of the subwavelength structure increases to 2.92. As a result, the peak wavelength shifts to 1585 nm even when the fiber is tilted to 20°, according to the simulation shown by the red curve in Fig. 4b. The peak efficiency, which reduces to -6.2 dB, is compromised too. However, the experimental results demonstrate a better efficiency of -5.2 dB, and the peak wavelength shifts back to 1545 nm. It is possibly due to the fact that the holes of subwavelength structures become larger when they are filled with SU-8.

Figure 5 shows the change of peak wavelength of grating couplers under different bending radii. The holes of subwavelength grating couplers are filled with SU-8. The data is captured under four different bending configurations. The input and output fibers are tilted at a fixed angle of 20°. For the longitudinal face-out bending (Fig. 5a), the peak wavelength shifts to longer wavelength, while for longitudinal face-in bending the peak wavelength shifts to shorter wavelength. The red curves in Fig. 5 are the simulation results by assuming that the evolution of the peak wavelength is mainly caused by the change of coupling angle. Taking the longitudinal face-out bending as an example, the coupling angle reduces along with the bending radius. According to the phase matching condition:

$$\frac{2\pi n_{neffavg}}{\lambda_0} = \frac{2\pi n_c \sin\theta_0}{\lambda_0} + \frac{2\pi}{\Lambda} \quad (4)$$

the peak wavelength $\lambda_0$can be calculated by:

$$\lambda_0 = \Lambda(n_{neffavg} - n_c \sin\theta_0) \quad (5)$$

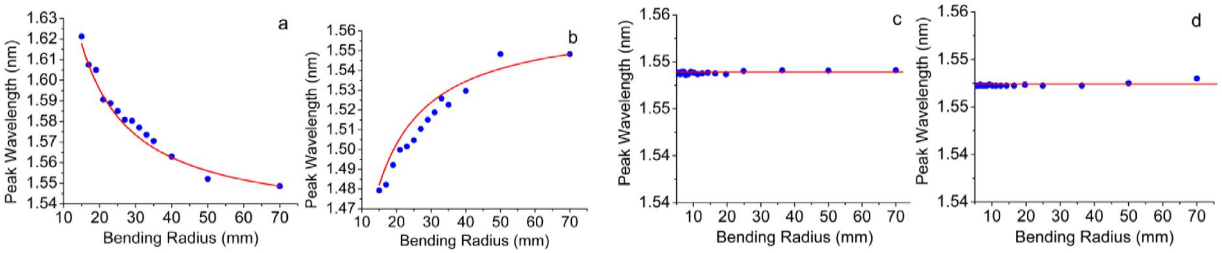

Figure 5 Peak wavelength shift of grating couplers under different bending conditions. a. longitudinal face-out bending. b. longitudinal face-in bending. c. transverse face-out bending. d. transverse face-in bending.

Here, Λ is the grating period. $n_{neffavg}$ is the average effective index of the grating coupler. n_c is the refractive index of the cladding, which equals to 1. θ_0 represents the fiber tilting angle, which can be estimated by approximately consider the bending curvature as part of a circle. The simulation matches the experimental results, as indicated in Fig. 5. For horizontal bending, the peak wavelength of the grating coupler stays the same due to the fact that the bending does not change any of the parameters in the phase matching condition.

To sum up, the experimental results prove that subwavelength grating couplers are an effective approach for the input and output coupling of flexible photonic circuits.

3.4 The characteristics of L13 cavity on flexible substrates

Figure 6a illustrates the photonic crystal micro cavity comprised of a linear photonic crystal micro cavity coupled with a W1 photonic crystal waveguide (PCW). The L13 cavity is formed by removing 13 holes from one side of the W1 waveguide. The lattice constant a is 392.5 nm and the hole radius r is 108 nm, giving a r/a of 0.275. W1 waveguide is formed by removing one row of holes along Γ–K direction. Silicon slab thickness is 250 nm. The dispersion relation of the W1 waveguide, simulated by three dimensional plane wave expansion (PWE), is shown in Fig. 6b. The cavity is located two rows away from

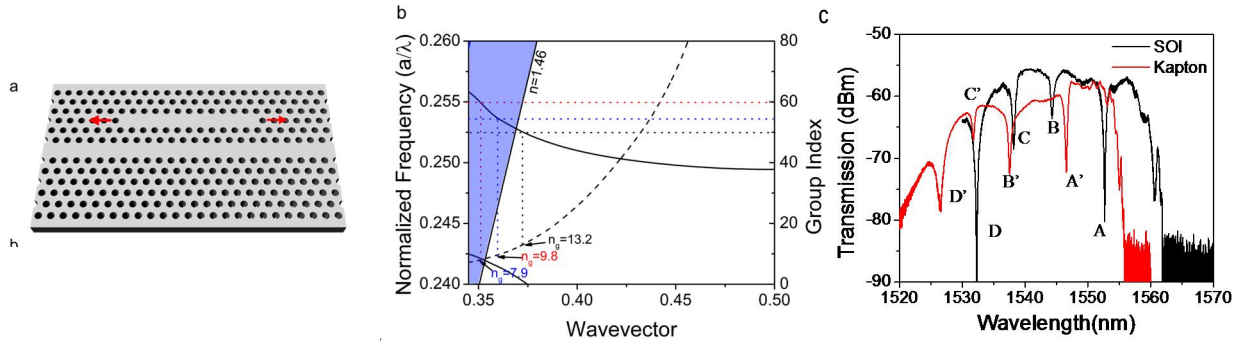

Figure 6 (a) The L13 cavity coupled with a W1 waveguide. (b) Dispersion relation diagram of the W1 PCW with the coupled L13 microcavity modes (water cladding). (c) The transmission spectra of the L13 cavity before (Black) and after transfer (Black). A~D and A'~D' are the resonances of the L13 cavity with water cladding

the W1 waveguide. The total quality factor Q_T of the resonance mode of a photonic crystal microcavity at frequency ω is given by[11]

$$\frac{1}{Q_T} = \frac{1}{Q_R} + \frac{1}{Q_i} \tag{6}$$

Here, $Q_T=wt_p$, $Q_R=wt_R$, *and* $Q_i=wt_i$. t_p, t_R, and t_i are photon lifetime, radiation lifetime, and intrinsic lifetime, respectively. [11] To increase Q_T, t_R is the parameter that is worth working on because t_i depends on the fabrication process. An abrupt change at the edges of the cavity causes radiation loss.[12] The holes at the two edges are moved outwards to obtain gentler confinement. Different amount of shift has been investigated to achieve the high Q. The most proper shift is 0.15a.

The transmission spectrum of the L13 cavity with water as top cladding is shown in Fig. 6c. The black curve is the transmission spectrum of the L13 cavity on SOI before transfer, showing four resonances. Resonance A is of most interest among all the resonant modes because it is close to the band edge of photonic crystal where the slow light effect is prominent and therefore, boosts the sensitivity most. The resonant wavelength of resonance A is at 1552.696 nm. The Q factor of the cavity can be estimated as:

$$Q = \frac{\lambda_o}{\Delta\lambda_{3dB}} \tag{7}$$

Here, λ_o is the resonant wavelength, and $\Delta\lambda_{3dB}$ is the 3 dB bandwidth. The Q factor of resonance A is therefore can be estimated to be ~ 9000. The existence of water, which is highly absorptive in the near infrared wavelength range, lowers the Q factor. The transmission spectrum of the L13 cavity transferred onto Kapton is shown by the red curve in Fig.6c. After transfer, resonance mode A blue shifts to a shorter wavelength of 1546.587 nm. There are a few factors that will affect the position of the resonant wavelength. On one hand, the photonic crystal holes are filled with SU-8. The average refractive index of photonic crystal increases, which pulls the guided mode in a dispersion relation diagram downwards, meaning the resonance wavelength is expected to red shift. On the other hand, the diameter of the holes increase during the transfer process because of the strain. The experimental results indicate that the change of hole diameters overrides the effect of the SU-8 filling. The Q factor after transfer is ~9000, which is very close to the value before transfer.

To test the chemical sensing capability, glycerol (1.46) is dropped on top of the cavity. The increase of the top cladding refractive index drags the guided mode down, and therefore the resonance shifts to longer wavelength, as shown in Fig. 7a. The Q factor increases to 30000

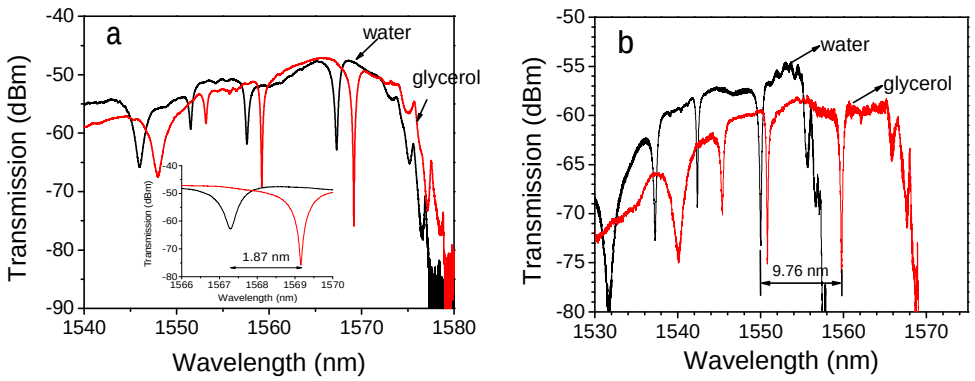

Figure 7 Refractive index sensing. a. photonic crystal holes are filled with SU-8. b. SU-8 inside photonic crystal holes are removed by oxygen plasma.

because glycerol has small absorption than water. The magnitude of shift is 1.87 nm, corresponding to a sensitivity of 13.4 nm/RIU. The sensitivity is rather low because the holes of photonic crystal are filled with SU-8, which prevent the electric field from interacting with the chemical. To solve the problem, the SU-8 filling into the photonic crystal holes are removed by oxygen plasma, exposing the electrical field to the chemical. The result of similar test performed on the modified sample is shown in Fig. 7b. The amount of shift drastically increases to 9.76 nm, corresponding to a sensitivity of 75 nm/RIU. It is comparable with the devices that have been demonstrated in other literature. [13]

3.5 Bending characteristic of the L13 microcavity

The bending characteristic of the L13 cavity is shown in Fig. 8. Four different bending scenarios have been investigated, longitudinal face-out bending in Fig. 8a, longitudinal face-in bending in Fig. 8b transverse face-out bending in Fig. 8c, and transverse face in bending in Fig. 8d. The behavior of the resonance wavelength under different bending situations is listed below. For face-out bending the resonant wavelength shifts to longer wavelength and for face in bending it shift to shorter wavelength. It is difficult to say which effect takes dominate roles, but it seems the deformation of photonic crystal holes matters most.

Figure 9 shows the sensitivity versus the bending radius. It is very interesting to notice that the sensitivity remains quite constant in all of the four bending scenario. In fact, the sensitivity even increases a little when the bending radius becomes small. It may because that when the bending radius reduces, the optical field will delocalized to be more close to the top surface, which will enhance the interaction between the chemical and the photons. All of the four figures show a sensitivity ~70 nm/RIU.

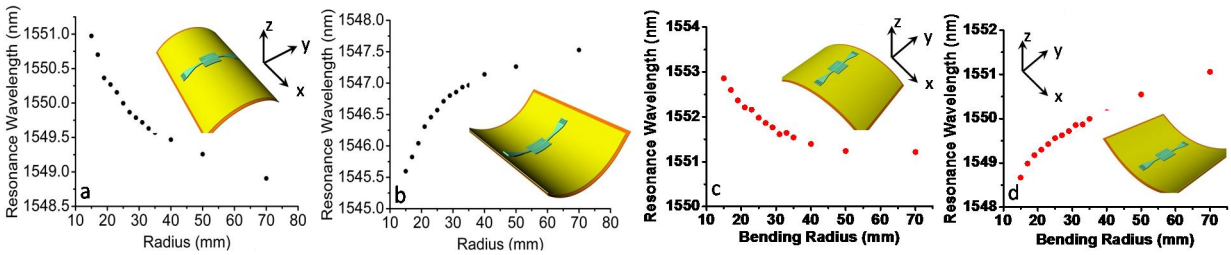

Figure 8 Resonance wavelength versus bending radius. (a) longitudinal face out bending; (b) longitudinal face in bending; (c) transverse face out bending; and (d) transverse face in bending

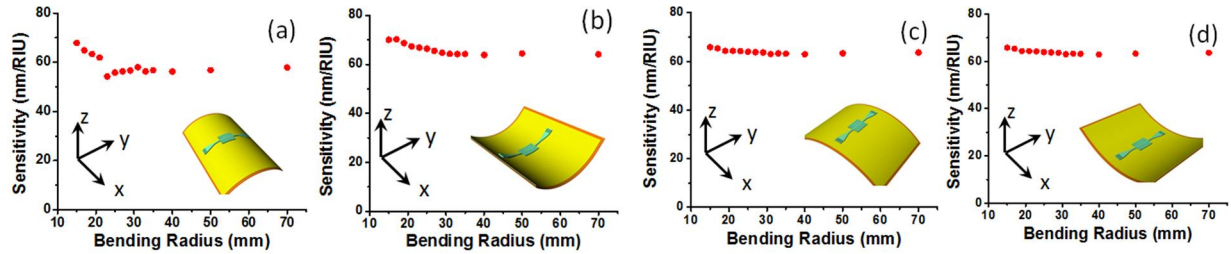

Figure 9 Sensitivity versus bending radius. (a) longitudinal face out bending; (b) longitudinal face in bending; (c) transverse face out bending; and (d) transverse face in bending

4. CONCLUSION

In this paper, we developed a transfer technique that can transfer silicon nanomembrane base devices onto flexible substrates. As an example, we demonstrated transferring L13 photonic crystal microcavities onto Kapton film. The performance of the transferred devices is comparable to those demonstrated on SOI platform. An experiment set up is designed to study the characteristics of the L13 cavity under four different types of bending scenario. The resonant wavelength shifts to longer wavelength when the nanomembrane is under tensile stress (face-out bending) and to shorter wavelength when the nanomembrane is under compressive stress (face-in bending). The sensitivity remains almost constant when the bending radius becomes small.

5. ACKNOWLEDGMENTS

This research was funded by Air Force Office of Scientific Research (AFOSR) STTR (Contract No. FA9550-11-C-0014), monitored by Dr. Gernot Pomrenke.

REFERENCES

[1] H. J. Yang, D. Y. Zhao, S. Chuwongin, J. H. Seo, W. Q. Yang, Y. C. Shuai, J. Berggren, M. Hammar, Z. Q. Ma, and W. D. Zhou, "Transfer-printed stacked nanomembrane lasers on silicon," Nat Photonics **6**, 615-620 (2012).

[2] H. J. Yang, D. Y. Zhao, J. H. Seo, S. Chuwongin, S. Kim, J. A. Rogers, Z. Q. Ma, and W. D. Zhou, "Broadband Membrane Reflectors on Glass," Ieee Photonic Tech L **24**, 476-478 (2012).

[3] X. C. Xu, H. Subbaraman, A. Hosseini, C. Y. Lin, D. Kwong, and R. T. Chen, "Stamp printing of silicon-nanomembrane-based photonic devices onto flexible substrates with a suspended configuration," Opt Lett **37**, 1020-1022 (2012).

[4] Y. Chen, H. Li, and M. Li, "Flexible and tunable silicon photonic circuits on plastic substrates," Sci Rep-Uk **2**(2012).

[5] L. Fan, L. T. Varghese, Y. Xuan, J. Wang, B. Niu, and M. H. Qi, "Direct fabrication of silicon photonic devices on a flexible platform and its application for strain sensing," Opt Express **20**, 20564-20575 (2012).

[6] K. Pfeiffer, M. Fink, G. Gruetzner, G. Bleidiessel, H. Schulz, and H. Scheer, "Multistep profiles by mix and match of nanoimprint and UV lithography," Microelectronic Engineering **57–58**, 381-387 (2001).

[7] T. Santeri and F. Sami, "Wafer-Level Bonding of MEMS Structures with SU-8 Epoxy Photoresist," Physica Scripta **2004**, 223 (2004).

[8] S. I. Park, J. H. Ahn, X. Feng, S. D. Wang, Y. G. Huang, and J. A. Rogers, "Theoretical and Experimental Studies of Bending of Inorganic Electronic Materials on Plastic Substrates," Adv Funct Mater **18**, 2673-2684 (2008).

[9] X. Xu, H. Subbaraman, J. Covey, D. Kwong, A. Hosseini, and R. T. Chen, "Complementary metal--oxide--semiconductor compatible high efficiency subwavelength grating couplers for silicon integrated photonics," Appl Phys Lett **101**, 031109-031104 (2012).

[10] H. Subbaraman, X. Xu, J. Covey, and R. T. Chen, "Efficient light coupling into in-plane semiconductor nanomembrane photonic devices utilizing a sub-wavelength grating coupler," Opt. Express **20**, 20659-20665 (2012).

[11] S. Chakravarty, Y. Zou, W. C. Lai, and R. T. Chen, "Slow light engineering for high Q high sensitivity photonic crystal microcavity biosensors in silicon," Biosens Bioelectron **38**, 170-176 (2012).

[12] Y. Akahane, T. Asano, B. S. Song, and S. Noda, "High-Q photonic nanocavity in a two-dimensional photonic crystal," Nature **425**, 944-947 (2003).
[13] W. C. Lai, S. Chakravarty, Y. Zou, and R. T. Chen, "Silicon nano-membrane based photonic crystal microcavities for high sensitivity bio-sensing," Opt Lett **37**, 1208-1210 (2012).